JACS
JOURNAL OF THE AMERICAN CHEMICAL SOCIETY

Article

pubs.acs.org/JACS

Seed Crystal Homogeneity Controls Lateral and Vertical Heteroepitaxy of Monolayer MoS_2 and WS_2

Youngdong Yoo, Zachary P. Degregorio, and James E. Johns*

Department of Chemistry, University of Minnesota, Minneapolis, Minnesota 55455, United States

Supporting Information

ABSTRACT: Heteroepitaxy between transition-metal dichalcogenide (TMDC) monolayers can fabricate atomically thin semiconductor heterojunctions without interfacial contamination, which are essential for next-generation electronics and optoelectronics. Here we report a controllable two-step chemical vapor deposition (CVD) process for lateral and vertical heteroepitaxy between monolayer WS_2 and MoS_2 on a *c*-cut sapphire substrate. Lateral and vertical heteroepitaxy can be selectively achieved by carefully controlling the growth of MoS_2 monolayers that are used as two-dimensional (2D) seed crystals. Using hydrogen as a carrier gas, we synthesize ultraclean MoS_2 monolayers, which enable lateral heteroepitaxial growth of monolayer WS_2 from the MoS_2 edges to create atomically coherent and sharp in-plane WS_2/MoS_2 heterojunctions. When no hydrogen is used, we obtain MoS_2 monolayers decorated with small particles along the edges, inducing vertical heteroepitaxial growth of monolayer WS_2 on top of the MoS_2 to form vertical WS_2/MoS_2 heterojunctions. Our lateral and vertical atomic layer heteroepitaxy steered by seed defect engineering opens up a new route toward atomically controlled fabrication of 2D heterojunction architectures.

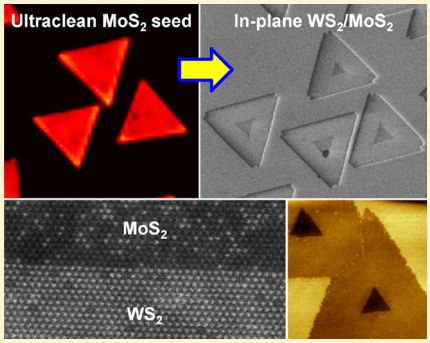

INTRODUCTION

Two-dimensional (2D) materials have emergent electronic and optical properties that are distinct from those of their bulk counterparts, as exemplified by graphene and its parent bulk material, graphite.[1−3] Monolayer transition-metal dichalcogendies (TMDCs) are a class of 2D materials that have direct band gaps and broken inversion symmetry, which are absent in the bulk.[4−8] These two combined properties have stimulated interest in using these materials for photodetectors, field effect transistors, and developing new devices to measure the physics of valley polarization.[9−15] Heterostructures between 2D materials exhibit junctions possessing new properties that are unobtainable from single-component 2D materials. In particular, heterojunctions composed of TMDC monolayers can serve as building blocks for next-generation optoelectronic devices, such as atomically thin solar cells and light-emitting diodes, due to their strong light−matter interactions.[14,16] The first heterojunctions between TMDC monolayers were created by mechanical exfoliation and vertical stacking.[17,18] Stacking WS_2/MoS_2 and stacking WSe_2/MoS_2 create type II heterostructures whose electronic properties depend sensitively on the twist angle between the two layers.[17−20] Recently, it was reported that both vertical and in-plane heterostructures of monolayer WS_2/MoS_2 can be synthesized using chemical vapor deposition (CVD) in a single step with MoO_3, W, tellurium, and sulfur precursors.[21]

Heteroepitaxy, the oriented growth of one crystalline material on another, can realize the scalable fabrication of atomically perfect heterojunctions without interfacial contamination.[22] In addition, heteroepitaxy can create in-plane TMDC heterojunctions that cannot be obtained by mechanical transfer methods. These in-plane junctions have intriguing optoelectronic properties, including a linearly abrupt p−n junction,[21] similar to junctions found in commercial field effect transistors. The previously reported methods for creating these heterojunctions utilized a single synthetic step,[21,23] which limits ultimate control over important features, such as particle size, shape, location, and junction width. A two-step process is highly desirable, because it could realize patterned 2D heterostructures and also achieve independent growth control of each component material. The advantages of controlled multistep growth have been previously reported for the synthesis of heterostructures composed of graphene and hexagonal boron nitride.[24−28]

Fabricating in-plane 2D heterostructures using two-step heteroepitaxy is challenging due to difficulties in controlling defects and contamination of the 2D seed crystals. Defects or particles persisting after the growth of the first material will serve as undesirable nucleation sites for depositing the second material.[29] Consequently, a two-step process to fabricate in-plane heterostructures composed of monolayer WS_2/MoS_2 requires extra care in preparing extremely clean surfaces and edges of the 2D seed crystals. Previous reports of CVD-grown TMDC monolayers, especially MoS_2, have shown that the surface and edges of individual monolayers are often contaminated by small particles.[30−37]

Received: June 26, 2015
Published: October 21, 2015

DOI: 10.1021/jacs.5b06643
J. Am. Chem. Soc. 2015, 137, 14281−14287

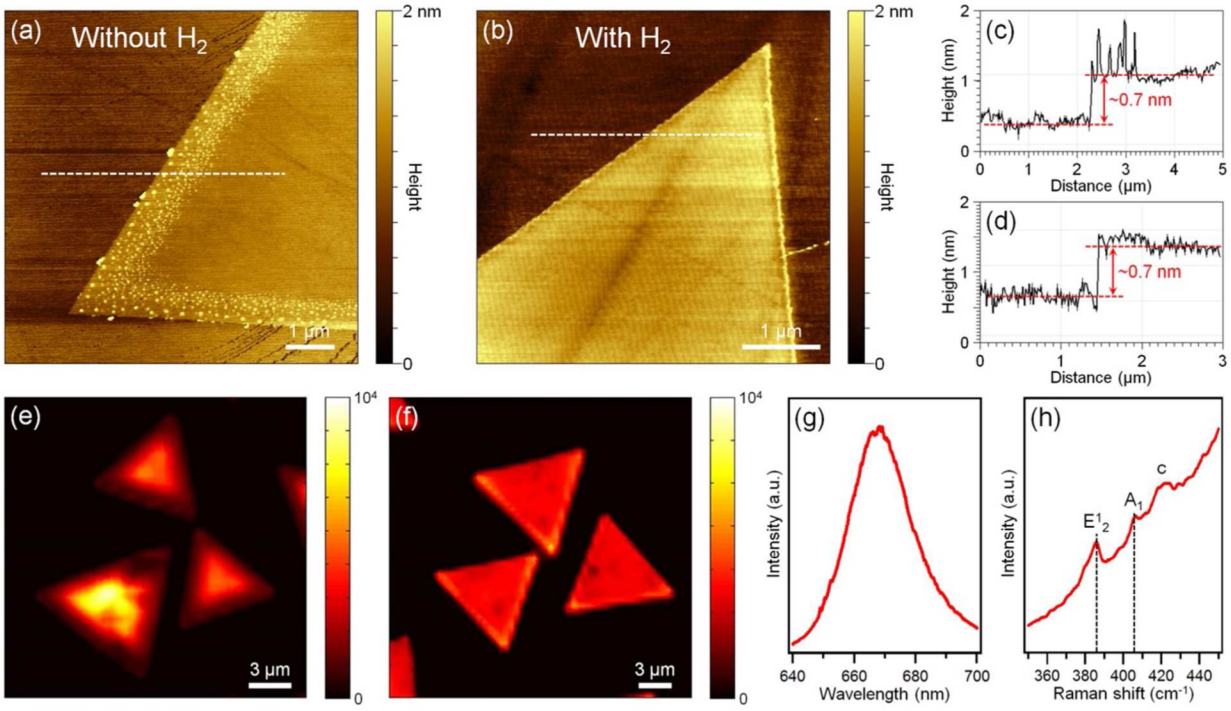

Figure 1. Monolayer MoS_2 crystals synthesized on *c*-cut sapphire without and with hydrogen gas. AFM height images of monolayer MoS_2 grown (a) without and (b) with hydrogen, respectively. (c, d) Height line profiles along the dotted white lines in panels a and b, respectively. PL intensity maps of monolayer MoS_2 grown (e) without and (f) with hydrogen, respectively. (g) PL and (h) Raman spectra of ultraclean monolayer MoS_2.

Here we report a two-step CVD process to selectively accomplish lateral and vertical heteroepitaxy between monolayer WS_2 and MoS_2 by careful growth control of monolayer MoS_2 seed crystals. We show that including hydrogen into the carrier gas results in ultraclean MoS_2 monolayers. These ultraclean flakes of MoS_2 suppress the nucleation and growth of additional vertical layers and enable the growth of lateral heteroepitaxial structures of monolayer WS_2 from the MoS_2 edges, creating atomically coherent and sharp in-plane WS_2/MoS_2 heterojunctions. When no hydrogen is used, we obtain MoS_2 monolayers decorated with small particles along the edge area. During the subsequent growth of WS_2, these particles nucleate heteroepitaxial growth of monolayer WS_2 on top of the MoS_2 seed to form vertical WS_2/MoS_2 heterojunctions with perfect alignment.

RESULTS AND DISCUSSION

We synthesize MoS_2 monolayers on *c*-cut sapphire using CVD with MoO_3 and S powder precursors and a carrier gas of Ar or H_2/Ar (4 sccm/20 sccm). Further details of the growth conditions are given in the Supporting Information (SI). In Figure 1, we compare triangular monolayer particles of MoS_2 grown with and without hydrogen in the carrier gas. Under typical CVD conditions without H_2, the edges of the MoS_2 flakes are decorated by small particles, as shown by atomic force microscopy (AFM) in Figure 1a,c. These particles have also been present in previously reported syntheses of MoS_2.[30−37] Inclusion of 4 sccm of H_2 into the carrier gas during the synthesis leads to the disappearance of these particles, as shown in Figures 1b,d. An additional high-resolution AFM height image of the ultraclean MoS_2 monolayer further confirms the ultraclean surface of the monolayer (Figure S1, SI). In both cases, the flakes are confirmed to be monolayer by the AFM profiles showing a height of approximately 0.7 nm, consistent with previous reports of monolayer MoS_2.[30−37] Raman spectroscopy also confirms the monolayer nature of the synthesized materials (Figure 1h). The Raman spectrum of MoS_2 shows two characteristic peaks, the out-of-plane vibration of the sulfur atoms (A_1) and the doubly degenerate in-plane vibrations of the Mo and S atoms (E_2).[38] The energy associated with these phonons changes with thickness, and the spectral separation of these two peaks has become a common tool for identifying the number of MoS_2 layers. For our MoS_2 flakes, we see a separation of 20.3 cm^{-1}, in agreement with previously reported syntheses of monolayer MoS_2[30−37] but slightly larger than exfoliated monolayer samples.[39] It is worth noting that the spectrum shown in Figure 1h was taken on resonance with the B exciton absorption band and that resonance Raman spectrum can induce spectral changes including line-broadening, a large fluorescence background, and additional non-zone centered modes. Due to the resonance, we observe additional modes including the mode indicated by "c" in Figure 1h, which are absent in the off-resonance Raman spectrum (Figure S2, SI).[38,40] To better measure the peak separation, we used an off-resonance 514.5 nm excitation (Figure S2, SI) which removes the spectral congestion and increases signal-to-noise, and we report a spectral separation of 17 cm^{-1}. The source of this decreased splitting is unknown. This could be due to enhanced substrate interactions, but further study is needed to explore this phenomenon. Photoluminescence (PL) spectroscopy further confirms that inclusion of hydrogen leads to a cleaner and more homogeneous material. Figure 1g shows a PL spectrum taken with 632.8 nm laser excitation at room temperature on ultraclean monolayer MoS_2, clearly showing strong A-exciton peak at 667 nm due to the direct band gap of monolayer MoS_2.[4,7] Parts e and f of Figure 1 show PL intensity maps of the emission from the A exciton (spectrum shown in Figure 1g) of monolayer MoS_2 grown without and with

DOI: 10.1021/jacs.5b06643
J. Am. Chem. Soc. 2015, 137, 14281−14287

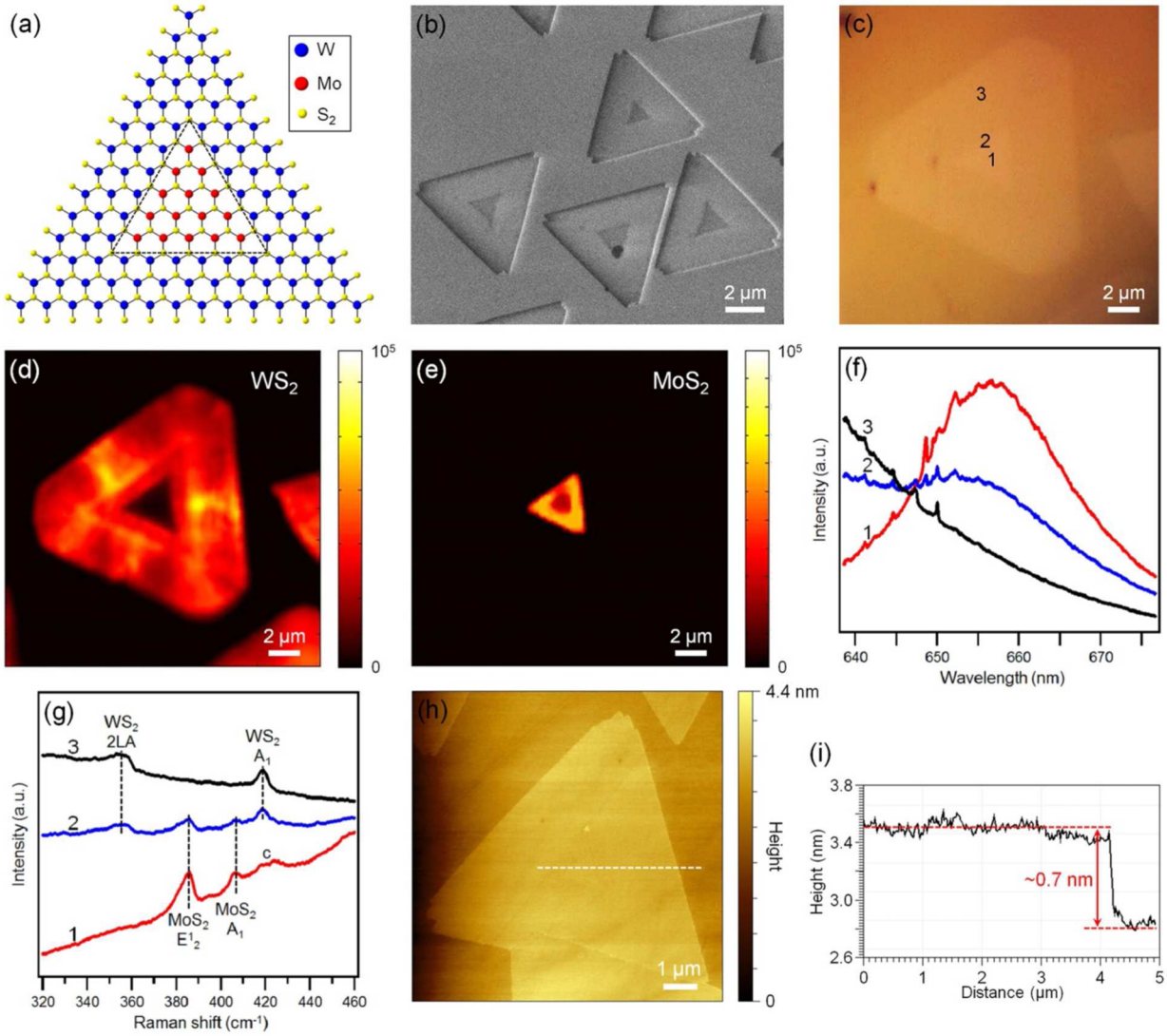

Figure 2. In-plane heteroepitaxial WS_2/MoS_2 monolayers synthesized from monolayer MoS_2 grown with hydrogen. (a) Atomic model of an in-plane heteroepitaxial junction between MoS_2 and WS_2. (b) SEM image of the in-plane heteroepitaxial monolayers. (c) Optical microscope image of the in-plane heteroepitaxial monolayer. (d and e) PL intensity mapping of WS_2 and MoS_2 from the in-plane heteroepitaxial monolayer, respectively. (f) PL and (g) Raman spectra taken from the points marked by 1−3 in panel c. (h) AFM height image of the in-plane heteroepitaxial monolayer. (i) Height line profile along the dotted white line in panel h.

hydrogen, respectively. In the flakes grown without H_2, the PL is spatially heterogeneous. Additionally, each flake shows a faint ribbon ∼1 μm wide with lower intensity due to partial quenching of the PL. When MoS_2 is grown with hydrogen, the PL map is highly uniform across each flake, indicating uniform chemical composition and electronic structure. Scanning electron microscopy (SEM) images of ultraclean and particle-decorated MoS_2 are shown in Figure S3 (SI).

When ultraclean MoS_2 flakes are used as seed particles in the growth of WS_2, we obtain in-plane, heteroepitaxial WS_2/MoS_2 monolayers, as shown in Figure 2. WS_2 was grown using previously reported low-pressure CVD methods at 1050 °C with WO_3 and S powder precursors in a carrier gas of H_2/Ar (5 sccm/60 sccm).[41] Figure 2a shows an atomic model of the in-plane heteroepitaxial WS_2/MoS_2 monolayer obtained by this two-step growth method. The SEM image in Figure 2b shows the in-plane, heteroepitaxial monolayers grown on a *c*-cut sapphire substrate. *c*-cut sapphire has both atomically flat surfaces as well as good lattice matching with MoS_2 and WS_2 and has been shown to improve the crystallinity of CVD-grown WS_2 and MoS_2.[42,43] The lattice mismatch is only 0.42 and 0.64% when we consider (3 × 3) MoS_2 or (3 × 3) WS_2 supercells on (2 × 2) sapphire, respectively. The in-plane, heteroepitaxial monolayers are oriented along two preferential directions on the substrate, indicating that the in-plane heteroepitaxial monolayers form epitaxially on *c*-cut sapphire. We frequently observe these oriented in-plane heterostructures on areas of the substrate when we use epitaxial MoS_2 monolayers as seeds.[42,43] The optical microscope image in Figure 2c shows an in-plane heteroepitaxial monolayer that was used for PL and Raman characterizations. Figure 2f shows PL spectra taken from the points marked by 1−3 in Figure 2c. The PL spectra taken from the inner triangle (point 1) and the outer ribbon (point 3) show strong PL signals of MoS_2 and WS_2 due to emission from the lowest energy exicitons (the "A" excitons) monolayer MoS_2 and WS_2, respectively.[4,7,39,44] The junction region of the in-plane heteroepitaxial monolayer exhibits PL signals of both WS_2 and MoS_2. PL spectra taken

DOI: 10.1021/jacs.5b06643
J. Am. Chem. Soc. 2015, 137, 14281−14287

under a laser excitation of 514.5 nm are shown in Figure S4 (SI). PL intensity maps of the A exciton from WS_2 and the A exciton from MoS_2 demonstrate the formation of the in-plane WS_2/MoS_2 junction (Figure 2d,e). The PL intensity variation in the maps could be attributed to nonuniform strain that can be induced by the difference of the thermal expansion coefficient between substrates and WS_2/MoS_2 or by the lattice mismatch between substrates and WS_2/MoS_2,[45,46] which can also lead to the variation of the Raman peak positions (Figure S5, SI). While Raman spectra taken from the inner triangle (point 1 in Figure 2c) shows E^1_2 and A_1 peaks of the MoS_2, Raman spectra from the outer ribbon (point 3 in Figure 2c) show peaks corresponding to the 2LA and A_1 phonons of monolayer WS_2 (Figure 2g). We observe Raman signals of both WS_2 and MoS_2 in the junction region. An AFM height image of the in-plane heterostructure (Figure 2h) and the line profile across the flake (Figure 2i) clearly show that the WS_2/MoS_2 flake is a single monolayer and that both materials are in the same plane with a height of 0.7 nm, the same as the monolayer MoS_2 seed crystals. Surprisingly, the AFM friction image clearly shows the lateral junction between MoS_2 and WS_2 (Figure S6, SI). In addition, Kelvin probe force microscopy (KPFM) data confirm that as-synthesized heterostructures have high-quality lateral junctions (Figure S7, SI).

We used scanning transmission electron microscopy (STEM) to characterize better the interface between these two materials and to demonstrate heteroepitaxy. High-angle annular dark field (HAADF) microscopy can provide contrast between the two materials based on the different scattering cross sections for Mo and W atoms (*Z*-contrast).[47] The atomic structure of the in-plane heteroepitaxial monolayer is characterized with atomic resolution by *Z*-contrast STEM microscopy imaging using an aberration-corrected STEM (FEI Titan, 60 kV). Figure 3a shows a low-magnification HAADF-STEM image of an in-plane heteroepitaxial monolayer. The junction between the outer ribbon of WS_2 and the inner triangle of MoS_2 is visible, but with low contrast. The magnified image of the dotted orange square in Figure 3a clearly shows the contrast between MoS_2 and WS_2 (Figure 3b). The image intensity at each point is determined by the spatially averaged atomic number and the thickness of the sample.[47] Since the average atomic number of WS_2 is higher than that of MoS_2, the WS_2 has higher image intensity (appears brighter) than the MoS_2 in dark-field imaging. Figure 3c shows an atomic-resolution HAADF-STEM image and the associated fast Fourier-transform (FFT) pattern of the junction region (inset) of the in-plane heterostructure, clearly showing the atomically sharp junction between WS_2 and MoS_2 along a zigzag direction. Despite growing the WS_2 at high temperatures, we see only minor annealing and elemental mixing across the interface between WS_2 and MoS_2 with a larger concentration of W substituted into the MoS_2 lattice than Mo substituted into the WS_2 lattice. The FFT patterns show only one set of hexagonal spots, demonstrating that the WS_2 grew from the MoS_2 edges with lattice coherence aided by the small lattice mismatch between WS_2 and MoS_2 (0.22%). Parts d and e of Figure 3 show atomic-resolution HAADF-STEM images and their FFT patterns taken from MoS_2 and WS_2 regions, respectively. Hexagonal lattices of MoS_2 and WS_2 are clearly visible without any substituted atoms. The orientation of the FFT patterns of the WS_2 region is the same as that of the MoS_2 region, further confirming the lattice coherence across the WS_2/MoS_2 boundary.

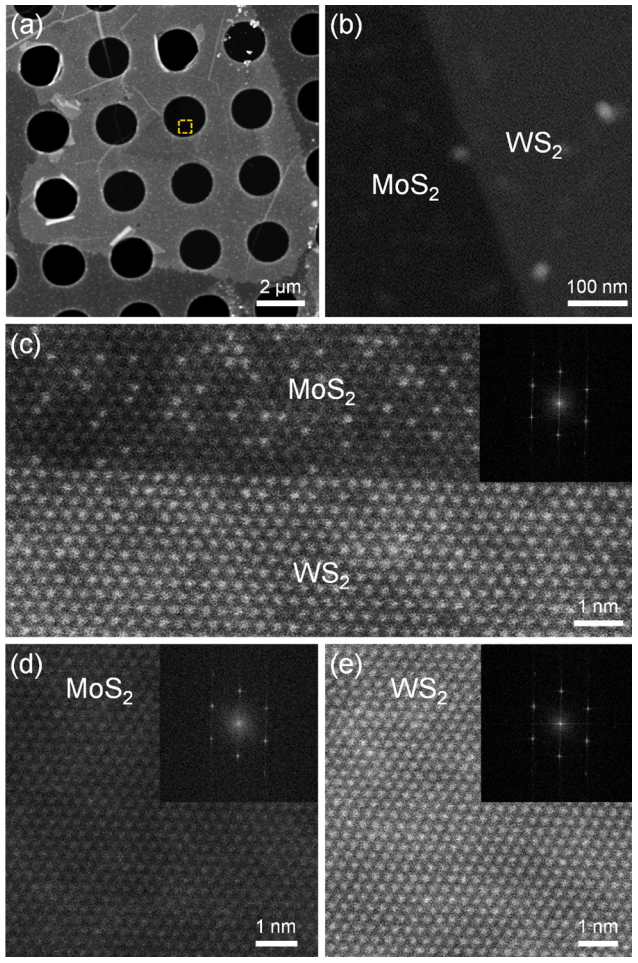

Figure 3. *Z*-Contrast HAADF-STEM images of the in-plane heteroepitaxial WS_2/MoS_2 monolayer. (a) Low-magnification HAADF-STEM image of the in-plane heteroepitaxial monolayer. (b) Magnified image of the dotted orange square in panel a. (c) Atomic-resolution HAADF-STEM image and its FFT pattern (inset) of the junction region of the in-plane heteroepitaxial monolayer. (d and e) Atomic-resolution HAADF-STEM images and their FFT patterns (inset) of the MoS_2 region and the WS_2 region, respectively, of the in-plane heteroepitaxial monolayer.

When we grow WS_2 using more conventional, particle-decorated MoS_2 monolayers as 2D seed crystals, we obtain vertically stacked WS_2/MoS_2 heterostructures surrounded by a ribbon of monolayer WS_2, as shown in Figure 4. SEM imaging shows a ribbon of WS_2 around the vertical heterostructures on the sapphire substrate (Figure 4a). We identify that these structures are vertically stacked using a combination of PL and Raman spectroscopy and AFM imaging. Figure 4b,c shows PL and Raman spectra taken from different locations of the vertical heterostructure shown in the inset of Figure 4b. The points marked by 1 and 2 indicate the center and edge of the vertical heterostructures, respectively, and each location shows the PL and Raman signals of both WS_2 and MoS_2. The vertical heterostructure shows a very weak PL signal because the PL signal is quenched by charge transfer between the WS_2 and the MoS_2.[17,48] The small triangular flakes in a neighborhood of the vertical heterostructures (marked as location 3) are identified as WS_2 monolayers by PL and Raman spectroscopy. These particles exhibit a strong PL signal of WS_2 due to a direct band gap of monolayer WS_2, and the Raman spectrum only shows

DOI: 10.1021/jacs.5b06643
J. Am. Chem. Soc. 2015, 137, 14281−14287

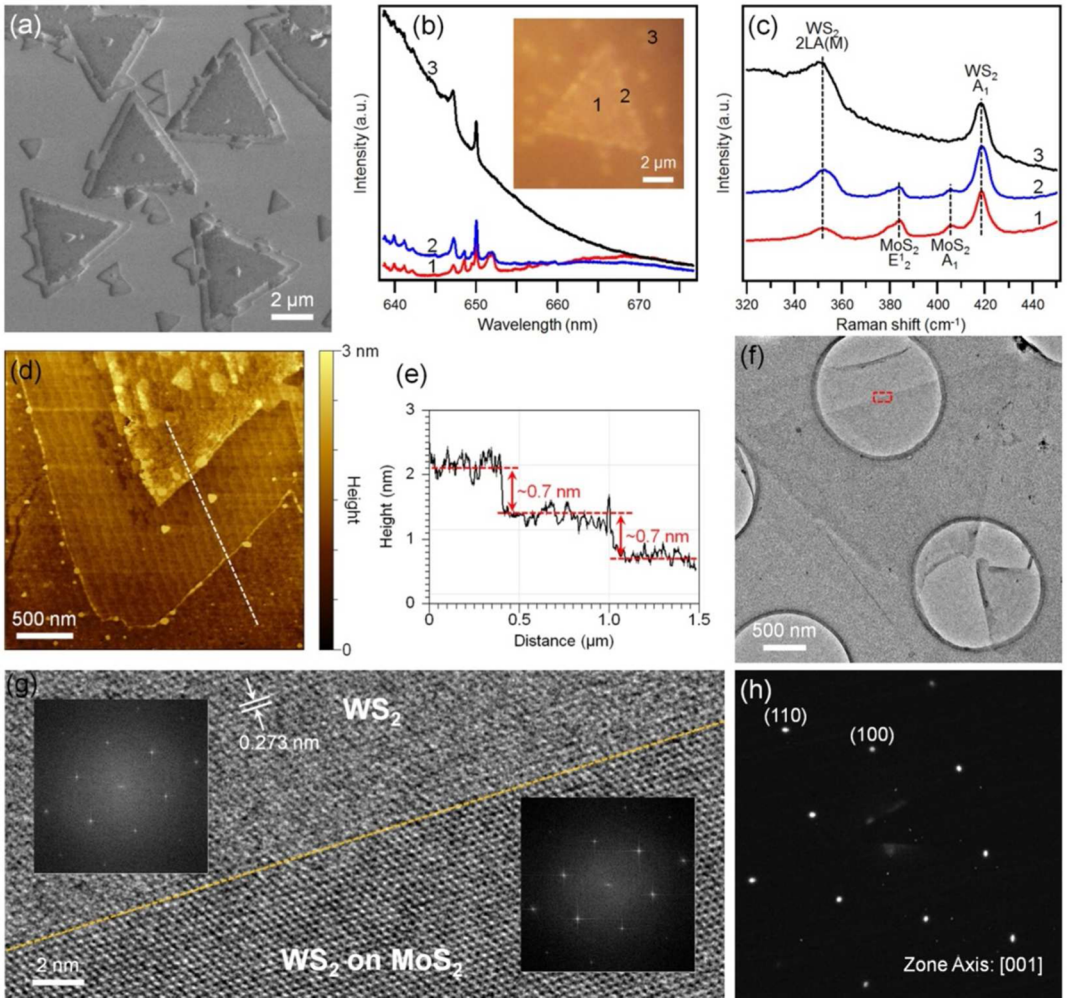

Figure 4. Vertical WS_2/MoS_2 heterostructures synthesized from monolayer MoS_2 grown without hydrogen. (a) SEM image of the vertical heterostructures. (b) PL and (c) Raman spectra taken from the points marked by 1−3 in the inset in panel b. The inset in panel b is an optical microscope image of a vertical heterostructure. (d) AFM height image of a vertical heterostructure. (e) Height line profile along the dotted white line in panel d. (f) Bright-field TEM image of the vertical heterostructure. (g) HRTEM image of the dotted red square in panel f. The insets are FFT patterns of the WS_2 region and the WS_2/MoS_2 region, respectively. (h) SAED pattern of the vertical heterostructure.

peaks from WS_2 and no evidence for MoS_2. The AFM height image and its line height profile show that the vertical WS_2/MoS_2 heterostructure possesses a thickness of about 1.4 nm and has a monolayer WS_2 ribbon with a thickness of about 0.7 nm (Figure 4d,e).

We used TEM imaging to better characterize the detailed crystal structure of the vertical heterostructures. Figure 4f is a bright-field TEM image of the vertical heterostructure, clearly showing the contrast between an inner triangle of the vertical WS_2/MoS_2 heterostructure and a ribbon of monolayer WS_2. The contrast of the HAADF-STEM images of the vertical heterostructure is the inverse of the contrast of the HAADF-STEM images of the in-plane heterostructure (Figure S8, SI). Figure 4g is a high-resolution TEM (HRTEM) image of the junction region between the WS_2 ribbon and the WS_2/MoS_2 taken in the region marked by the dotted red square of Figure 4f, showing the hexagonal lattices of the WS_2 and the WS_2/MoS_2. In the WS_2 region, the lattice spacing of the planes perpendicular to the junction direction is 0.273 nm, which is consistent with the spacing of the (100) planes of WS_2. The orientation of the FFT patterns of the WS_2 region is the same as that of the WS_2/MoS_2 region, confirming that the ribbon of monolayer WS_2 forms epitaxially onto the edge of the vertical WS_2/MoS_2 heterostructure. The selected area electron diffraction (SAED) pattern of the vertical WS_2/MoS_2 heterostructure shows only a single set of hexagonal diffraction spots (Figure 4h). This confirms that the WS_2 grows on the top of the MoS_2 with the same stacking orientation, demonstrating vertical heteroepitaxy between WS_2 and MoS_2.

We believe that in-plane growth of WS_2 ribbons around monolayer MoS_2 is kinetically controlled, because vertical heterostructures are thermodynamically more stable than in-plane heterostructures, as previously reported.[21] The commonly accepted mechanisms for the formation of MoS_2 and WS_2 monolayers from their oxide precursors are identical. Thermal reduction of the trioxide produces a volatile suboxide.[49−51] This suboxide can adsorb onto, diffuse along, and desorb from the substrate unless it encounters a nucleation site where it will subsequently sulfurize, forming MoS_2 or WS_2, respectively. The suboxide clusters can be supplied to the MoS_2 seed flakes by direct impingement from the vapor or by surface diffusion from the substrate. It has been reported that surface diffusion can be the major supply of clusters under high flux conditions while direct impingement can be a major supply of

DOI: 10.1021/jacs.5b06643
J. Am. Chem. Soc. 2015, 137, 14281−14287

clusters under low flux conditions.[52] The suboxide clusters supplied by surface diffusion from the substrate, arriving at the edges of the MoS_2 seed flakes, will contribute mostly to the in-plane growth of WS_2 ribbons around monolayer MoS_2, because the anisotropic flows of materials can induce the anisotropic growth.[53] Thus, all the WS_2 growths described above were performed under high flux conditions. By contrast, we obtain vertical WS_2/MoS_2 heterostructures possessing no WS_2 ribbons under low flux conditions (Figure S9, SI). Under our kinetically controlled reaction conditions, monolayer WS_2 grows laterally from the edges of monolayer MoS_2, because these edge sites are the only sites active for nucleation when we use ultraclean MoS_2 monolayers on *c*-cut sapphire as seeds.[54] This kinetic process is responsible for the formation of the lateral, in-plane heterostructures reported here. When particle-decorated MoS_2 monolayers are used as seeds, not only the MoS_2 edges but also the particles on the MoS_2 surface will serve as nucleation sites, leading to the formation of vertical WS_2/MoS_2 heterostructures with a ribbon of monolayer WS_2.

The ability to control the competitive growth between in-plane and vertical heterostructures hinges on the ability to control the cleanliness of the MoS_2 seed flakes. The small particles that exist on the surface and edges of the monolayer MoS_2 synthesized without hydrogen should be mostly MoS_2 formed by sulfurization of small molybdenum oxide particles. Tiny clusters of molybdenum suboxide will be continuously supplied to the substrate during the reaction. Although most of the suboxide clusters will contribute to the growth of monolayers or desorb from the substrate by re-evaporation due to the high temperature of the substrate, some of the suboxide clusters will aggregate and form more stable small molybdenum oxide particles. During this process, the edge regions of the monolayer MoS_2 could serve as preferential nucleation sites because the edge regions could be sulfur-deficient when no hydrogen is used, as was recently reported.[55] These particles will subsequently react with sulfur vapor to form small MoS_2 particles. The stability of the suboxide particles is lowered in the presence of highly reducing hydrogen gas.[49,51] The reduction of suboxide particles by H_2 will revolatilize the precursors, leaving the basal plane of the MoS_2 flake clean of debris. In addition, we believe that monolayer MoS_2 synthesized with hydrogen has highly homogeneous edges without sulfur deficiency, because hydrogen can improve the quality of the edges of monolayer TMDCs significantly.[41,56]

CONCLUSION

In summary, we demonstrate that by carefully controlling contamination and defects of 2D seed crystals we can selectively achieve lateral and vertical heteroepitaxy between monolayer WS_2 and MoS_2 on a *c*-cut sapphire substrate. We show that hydrogen gas plays an important role in removing small particles contaminating MoS_2 monolayer seeds. When we use hydrogen as a carrier gas, we synthesize ultraclean MoS_2 monolayers, which can be used as seeds for lateral heteroepitaxial growth of monolayer WS_2 to form atomically coherent and sharp in-plane WS_2/MoS_2 heterojunctions. When no hydrogen is used, we obtain particle-decorated MoS_2 monolayers, which serve as seeds for vertical heteroepitaxial growth of monolayer WS_2, producing vertical WS_2/MoS_2 heterojunctions. This two-step synthesis can then serve as a building block for making abrupt junctions in 2D materials, as patterned junctions in 2D materials and as platforms for further exploring the interesting electronic and optical properties of these materials.

ASSOCIATED CONTENT

Supporting Information

The Supporting Information is available free of charge on the ACS Publications website at DOI: 10.1021/jacs.5b06643.

Synthesis of ultraclean and particle-decorated MoS_2 monolayers; synthetic details of in-plane and vertical WS_2/MoS_2 heterostructures; transfer of WS_2/MoS_2 heterostructures onto a TEM grid; characterization (STEM, TEM, AFM, KPFM, Raman, PL, and SEM measurements); high-resolution AFM height image of monolayer MoS_2 grown with hydrogen; Raman spectra and Lorentz fitting results for monolayer MoS_2; SEM images of monolayer MoS_2 grown with and without hydrogen; PL spectra of in-plane heterostructures taken under a laser excitation of 514.5 nm; Raman peak position mapping of in-plane heterostructures; AFM friction image of the same flake shown in Figure 2g; KPFM data of in-plane heterostructures; vertical heterostructures synthesized under low flux conditions (PDF)

AUTHOR INFORMATION

Corresponding Author

*jjohns@umn.edu

Notes

The authors declare no competing financial interest.

ACKNOWLEDGMENTS

We thank Jason Myers for his help in acquiring the aberration-corrected TEM images. This work was primarily supported by startup funding from the University of Minnesota. This work was supported partially by the National Science Foundation through the University of Minnesota MRSEC under Award Number DMR-1420013. Part of this work was carried out in the College of Science and Engineering Characterization Facility, University of Minnesota, which has received capital equipment funding from the NSF through the UMN MRSEC program under Award Number DMR-420013.

REFERENCES

(1) Geim, A. K.; Novoselov, K. S. *Nat. Mater.* **2007**, *6*, 183−191.
(2) Geim, A. K. *Science* **2009**, *324*, 1530−1534.
(3) Li, X. S.; Magnuson, C. W.; Venugopal, A.; Tromp, R. M.; Hannon, J. B.; Vogel, E. M.; Colombo, L.; Ruoff, R. S. *J. Am. Chem. Soc.* **2011**, *133*, 2816−2819.
(4) Mak, K. F.; Lee, C.; Hone, J.; Shan, J.; Heinz, T. F. *Phys. Rev. Lett.* **2010**, *105*, 136805.
(5) Wang, Q. H.; Kalantar-Zadeh, K.; Kis, A.; Coleman, J. N.; Strano, M. S. *Nat. Nanotechnol.* **2012**, *7*, 699−712.
(6) Xiao, D.; Liu, G. B.; Feng, W. X.; Xu, X. D.; Yao, W. *Phys. Rev. Lett.* **2012**, *108*, 196802.
(7) Splendiani, A.; Sun, L.; Zhang, Y. B.; Li, T. S.; Kim, J.; Chim, C. Y.; Galli, G.; Wang, F. *Nano Lett.* **2010**, *10*, 1271−1275.
(8) Li, H.; Duan, X.; Wu, X.; Zhuang, X.; Zhou, H.; Zhang, Q.; Zhu, X.; Hu, W.; Ren, P.; Guo, P.; Ma, L.; Fan, X.; Wang, X.; Xu, J.; Pan, A.; Duan, X. *J. Am. Chem. Soc.* **2014**, *136*, 3756−3759.
(9) Kiriya, D.; Tosun, M.; Zhao, P.; Kang, J. S.; Javey, A. *J. Am. Chem. Soc.* **2014**, *136*, 7853−7856.
(10) Mak, K. F.; He, K. L.; Shan, J.; Heinz, T. F. *Nat. Nanotechnol.* **2012**, *7*, 494−498.

DOI: 10.1021/jacs.5b06643
J. Am. Chem. Soc. 2015, 137, 14281−14287

(11) Mak, K. F.; McGill, K. L.; Park, J.; McEuen, P. L. *Science* **2014**, *344*, 1489−1492.
(12) Xu, X. D.; Yao, W.; Xiao, D.; Heinz, T. F. *Nat. Phys.* **2014**, *10*, 343−350.
(13) Zhang, Y. J.; Oka, T.; Suzuki, R.; Ye, J. T.; Iwasa, Y. *Science* **2014**, *344*, 725−728.
(14) Lopez-Sanchez, O.; Lembke, D.; Kayci, M.; Radenovic, A.; Kis, A. *Nat. Nanotechnol.* **2013**, *8*, 497−501.
(15) Radisavljevic, B.; Radenovic, A.; Brivio, J.; Giacometti, V.; Kis, A. *Nat. Nanotechnol.* **2011**, *6*, 147−50.
(16) Britnell, L.; Ribeiro, R. M.; Eckmann, A.; Jalil, R.; Belle, B. D.; Mishchenko, A.; Kim, Y. J.; Gorbachev, R. V.; Georgiou, T.; Morozov, S. V.; Grigorenko, A. N.; Geim, A. K.; Casiraghi, C.; Castro Neto, A. H.; Novoselov, K. S. *Science* **2013**, *340*, 1311−1314.
(17) Hong, X. P.; Kim, J.; Shi, S. F.; Zhang, Y.; Jin, C. H.; Sun, Y. H.; Tongay, S.; Wu, J. Q.; Zhang, Y. F.; Wang, F. *Nat. Nanotechnol.* **2014**, *9*, 682−686.
(18) Lee, C. H.; Lee, G. H.; van der Zande, A. M.; Chen, W. C.; Li, Y. L.; Han, M. Y.; Cui, X.; Arefe, G.; Nuckolls, C.; Heinz, T. F.; Guo, J.; Hone, J.; Kim, P. *Nat. Nanotechnol.* **2014**, *9*, 676−681.
(19) Tongay, S.; Fan, W.; Kang, J.; Park, J.; Koldemir, U.; Suh, J.; Narang, D. S.; Liu, K.; Ji, J.; Li, J. B.; Sinclair, R.; Wu, J. Q. *Nano Lett.* **2014**, *14*, 3185−3190.
(20) Zhu, X.; Monahan, N. R.; Gong, Z.; Zhu, H.; Williams, K. W.; Nelson, C. A. *J. Am. Chem. Soc.* **2015**, *137*, 8313−8320.
(21) Gong, Y. J.; Lin, J. H.; Wang, X. L.; Shi, G.; Lei, S. D.; Lin, Z.; Zou, X. L.; Ye, G. L.; Vajtai, R.; Yakobson, B. I.; Terrones, H.; Terrones, M.; Tay, B. K.; Lou, J.; Pantelides, S. T.; Liu, Z.; Zhou, W.; Ajayan, P. M. *Nat. Mater.* **2014**, *13*, 1135−1142.
(22) Vispute, R. D.; Talyansky, V.; Choopun, S.; Sharma, R. P.; Venkatesan, T.; He, M.; Tang, X.; Halpern, J. B.; Spencer, M. G.; Li, Y. X.; Salamanca-Riba, L. G.; Iliadis, A. A.; Jones, K. A. *Appl. Phys. Lett.* **1998**, *73*, 348−350.
(23) Zhang, X.-Q.; Lin, C.-H.; Tseng, Y.-W.; Huang, K.-H.; Lee, Y.-H. *Nano Lett.* **2015**, *15*, 410−415.
(24) Levendorf, M. P.; Kim, C. J.; Brown, L.; Huang, P. Y.; Havener, R. W.; Muller, D. A.; Park, J. *Nature* **2012**, *488*, 627−632.
(25) Liu, L.; Park, J.; Siegel, D. A.; McCarty, K. F.; Clark, K. W.; Deng, W.; Basile, L.; Idrobo, J. C.; Li, A. P.; Gu, G. *Science* **2014**, *343*, 163−167.
(26) Liu, Z.; Ma, L. L.; Shi, G.; Zhou, W.; Gong, Y. J.; Lei, S. D.; Yang, X. B.; Zhang, J. N.; Yu, J. J.; Hackenberg, K. P.; Babakhani, A.; Idrobo, J. C.; Vajtai, R.; Lou, J.; Ajayan, P. M. *Nat. Nanotechnol.* **2013**, *8*, 119−124.
(27) Kim, S. M.; Hsu, A.; Araujo, P. T.; Lee, Y. H.; Palacios, T.; Dresselhaus, M.; Idrobo, J. C.; Kim, K. K.; Kong, J. *Nano Lett.* **2013**, *13*, 933−941.
(28) Shin, H. C.; Jang, Y.; Kim, T. H.; Lee, J. H.; Oh, D. H.; Ahn, S. J.; Moon, Y.; Park, J. H.; Yoo, S. J.; Park, C. Y.; Whang, D.; Yang, C. W.; Ahn, J. R. *J. Am. Chem. Soc.* **2015**, *137*, 6897−6905.
(29) Heo, H.; Sung, J. H.; Jin, G.; Ahn, J. H.; Kim, K.; Lee, M. J.; Cha, S.; Choi, H.; Jo, M. H. *Adv. Mater.* **2015**, *27*, 3803−3810.
(30) Liu, Y. N.; Ghosh, R.; Wu, D.; Ismach, A.; Ruoff, R.; Lai, K. J. *Nano Lett.* **2014**, *14*, 4682−4686.
(31) Ling, X.; Lee, Y. H.; Lin, Y. X.; Fang, W. J.; Yu, L. L.; Dresselhaus, M. S.; Kong, J. *Nano Lett.* **2014**, *14*, 464−472.
(32) Kim, I. S.; Sangwan, V. K.; Jariwala, D.; Wood, J. D.; Park, S.; Chen, K. S.; Shi, F. Y.; Ruiz-Zepeda, F.; Ponce, A.; Jose-Yacaman, M.; Dravid, V. P.; Marks, T. J.; Hersam, M. C.; Lauhon, L. J. *ACS Nano* **2014**, *8*, 10551−10558.
(33) Song, I.; Park, C.; Hong, M.; Baik, J.; Shin, H.-J.; Choi, H. C. *Angew. Chem., Int. Ed.* **2014**, *53*, 1266−1269.
(34) Zhang, C. D.; Johnson, A.; Hsu, C. L.; Li, L. J.; Shih, C. K. *Nano Lett.* **2014**, *14*, 2443−2447.
(35) Wu, S. F.; Huang, C. M.; Aivazian, G.; Ross, J. S.; Cobden, D. H.; Xu, X. D. *ACS Nano* **2013**, *7*, 2768−2772.
(36) Ji, Q.; Zhang, Y.; Gao, T.; Ma, D.; Liu, M.; Chen, Y.; Qiao, X.; Tan, P. H.; Kan, M.; Feng, J.; Sun, Q.; Liu, Z. *Nano Lett.* **2013**, *13*, 3870−3877.
(37) Wang, X. S.; Feng, H. B.; Wu, Y. M.; Jiao, L. Y. *J. Am. Chem. Soc.* **2013**, *135*, 5304−5307.
(38) Li, H.; Zhang, Q.; Yap, C. C. R.; Tay, B. K.; Edwin, T. H. T.; Olivier, A.; Baillargeat, D. *Adv. Funct. Mater.* **2012**, *22*, 1385−1390.
(39) Ye, M.; Winslow, D.; Zhang, D.; Pandey, R.; Yap, Y. *Photonics* **2015**, *2*, 288−307.
(40) Chakraborty, B.; Matte, H. S. S. R.; Sood, A. K.; Rao, C. N. R. *J. Raman Spectrosc.* **2013**, *44*, 92−96.
(41) Zhang, Y.; Zhang, Y. F.; Ji, Q. Q.; Ju, J.; Yuan, H. T.; Shi, J. P.; Gao, T.; Ma, D. L.; Liu, M. X.; Chen, Y. B.; Song, X. J.; Hwang, H. Y.; Cui, Y.; Liu, Z. F. *ACS Nano* **2013**, *7*, 8963−8971.
(42) Dumcenco, D.; Ovchinnikov, D.; Marinov, K.; Lazic, P.; Gibertini, M.; Marzari, N.; Sanchez, O. L.; Kung, Y. C.; Krasnozhon, D.; Chen, M. W.; Bertolazzi, S.; Gillet, P.; Fontcuberta i Morral, A.; Radenovic, A.; Kis, A. *ACS Nano* **2015**, *9*, 4611−4620.
(43) Ji, Q. Q.; Kan, M.; Zhang, Y.; Guo, Y.; Ma, D. L.; Shi, J. P.; Sun, Q.; Chen, Q.; Zhang, Y. F.; Liu, Z. F. *Nano Lett.* **2015**, *15*, 198−205.
(44) Gutierrez, H. R.; Perea-Lopez, N.; Elias, A. L.; Berkdemir, A.; Wang, B.; Lv, R.; Lopez-Urias, F.; Crespi, V. H.; Terrones, H.; Terrones, M. *Nano Lett.* **2013**, *13*, 3447−54.
(45) Liu, Z.; Amani, M.; Najmaei, S.; Xu, Q.; Zou, X. L.; Zhou, W.; Yu, T.; Qiu, C. Y.; Birdwell, A. G.; Crowne, F. J.; Vajtai, R.; Yakobson, B. I.; Xia, Z. H.; Dubey, M.; Ajayan, P. M.; Lou, J. *Nat. Commun.* **2014**, *5*, 5246.
(46) Li, M. Y.; Shi, Y.; Cheng, C. C.; Lu, L. S.; Lin, Y. C.; Tang, H. L.; Tsai, M. L.; Chu, C. W.; Wei, K. H.; He, J. H.; Chang, W. H.; Suenaga, K.; Li, L. J. *Science* **2015**, *349*, 524−528.
(47) Krivanek, O. L.; Chisholm, M. F.; Nicolosi, V.; Pennycook, T. J.; Corbin, G. J.; Dellby, N.; Murfitt, M. F.; Own, C. S.; Szilagyi, Z. S.; Oxley, M. P.; Pantelides, S. T.; Pennycook, S. J. *Nature* **2010**, *464*, 571−574.
(48) Yu, Y.; Hu, S.; Su, L.; Huang, L.; Liu, Y.; Jin, Z.; Purezky, A. A.; Geohegan, D. B.; Kim, K. W.; Zhang, Y.; Cao, L. *Nano Lett.* **2015**, *15*, 486−491.
(49) Kim, B. S.; Kim, E. Y.; Jeon, H. S.; Lee, H. I.; Lee, J. C. *Mater. Trans.* **2008**, *49*, 2147−2152.
(50) Leisegang, T.; Levin, A. A.; Walter, J.; Meyer, D. C. *Cryst. Res. Technol.* **2005**, *40*, 95−105.
(51) Schulmeyer, W. V.; Ortner, H. M. *Int. J. Refract. Hard Met.* **2002**, *20*, 261−269.
(52) Yoo, Y.; Seo, K.; Han, S.; Varadwaj, K. S.; Kim, H. Y.; Ryu, J. H.; Lee, H. M.; Ahn, J. P.; Ihee, H.; Kim, B. *Nano Lett.* **2010**, *10*, 432−438.
(53) Henry, C. R. *Prog. Surf. Sci.* **2005**, *80*, 92−116.
(54) Helveg, S.; Lauritsen, J. V.; Laegsgaard, E.; Stensgaard, I. I.; Norskov, J. K.; Clausen, B. S.; Topsoe, H.; Besenbacher, F. *Phys. Rev. Lett.* **2000**, *84*, 951−954.
(55) Bao, W.; Borys, N. J.; Ko, C.; Suh, J.; Fan, W.; Thron, A.; Zhang, Y.; Buyanin, A.; Zhang, J.; Cabrini, S.; Ashby, P. D.; Weber-Bargioni, A.; Tongay, S.; Aloni, S.; Ogletree, D. F.; Wu, J.; Salmeron, M. B.; Schuck, P. J. *Nat. Commun.* **2015**, *6*, 7993.
(56) Huang, J. K.; Pu, J.; Hsu, C. L.; Chiu, M. H.; Juang, Z. Y.; Chang, Y. H.; Chang, W. H.; Iwasa, Y.; Takenobu, T.; Li, L. J. *ACS Nano* **2014**, *8*, 923−930.

DOI: 10.1021/jacs.5b06643
J. Am. Chem. Soc. 2015, 137, 14281−14287